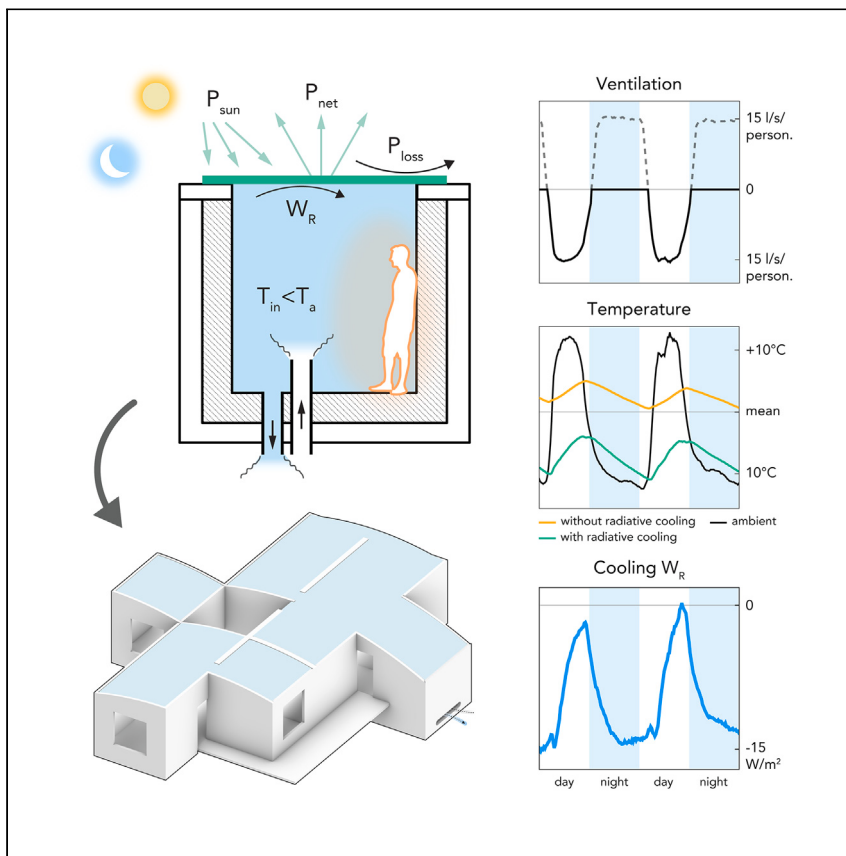


Article

Passive radiative cooling to sub-ambient temperatures inside naturally ventilated buildings



Fortin et al. show how 24-h radiative cooling to the blackbody universe can augment passive thermoregulation for buildings in hot and dry climates. Their field experiment combines radiative cooling and buoyancy forces to spontaneously cool and ventilate a heated enclosure, balancing sub-ambient temperatures with healthy air changes.

Remy Fortin, Jyotirmoy Mandal,
Aaswath P. Raman, Salmaan
Craig

salmaan.craig@mcgill.ca

Highlights

How to passively maintain sub-ambient temperatures in well-ventilated buildings

Combines radiative cooling with thermal mass and temperature-driven ventilation

Test box far cooler than ambient and gold standard (same air changes, heat gains)

Results scalable to per-person heat balance and ventilation needs

Article

Passive radiative cooling to sub-ambient temperatures inside naturally ventilated buildings

Remy Fortin,¹ Jyotirmoy Mandal,² Aaswath P. Raman,³ and Salmaan Craig^{1,4,5,*}

SUMMARY

Daytime radiative cooling materials can help prevent overheating by keeping exterior roof surfaces cool, but can they passively reject heat from inside buildings, overcoming thermal gains from healthy air changes without mechanical assistance? Here we report how to produce sub-ambient interior temperatures by balancing terrestrial radiative cooling with temperature-driven ventilation and thermal mass. We present a field study with model enclosures replicating one occupant's heat balance and air changes. The reference box represents a "gold standard" in passive cooling, with thermal mass and night ventilation offsetting internal heat gains. The test box maintains an interior temperature of 3.9°C below the mean prevailing exterior temperature and 8.9°C below the gold standard, despite being actively heated from within and venting seven air changes per hour during the day. We also show with a calibrated model how to improve the cooling and ventilation performance while scaling the results to actual buildings.

INTRODUCTION

Climate change is driving demand for mechanical air-conditioning while the greenhouse gas emissions associated with these systems, including those from refrigerants, further heat the planet.^{1–4} Several breakthroughs in passive radiative cooling materials, which reflect sunshine like a mirror while emitting infrared heat into cold outer space through the atmospheric window, have been made recently.^{5–12} These materials and coatings can mitigate urban heat islands and augment mechanical heat rejection from inside buildings.^{13–18} They have been added to the outside surface of insulated roofs, improving the energy efficiency of entire building stocks.^{15–17,19} However, true cooling entails removing heat, which is more challenging than improving heat protection.^{20,21}

On a hot day, these surface materials can reduce the temperature difference across the exterior insulation, but, if the temperature gradient flips in the direction of cooling, the insulation limits outward heat flow. Interior heat rejection is even more challenging in the aftermath of the COVID-19 pandemic now that healthy ventilation is a priority.²² Outdoor air exchanges can soon become the dominant source of heating when trying to cool the indoors below the ambient temperature.

Passive heat rejection requires selectively harnessing useful heat flows while negating ones that are harmful. This design challenge captured the imagination of many well-known architects and engineers in the twentieth century. Felix Trombe, a pioneer of radiative cooling, explored removing insulation from sky-facing surfaces to reject heat with terrestrial radiation from inside test boxes and experimental buildings (Figures 1A–1C).^{16,23–25,26} These "cold house" experiments were conducted in the French Pyrenees during the 1960s. In the most developed experiment (Figures 1B and 1C), the cooling facade was oriented north and tilted slightly upward. The facade was made of

¹School of Architecture, McGill University, Montréal, QC H3A 0C2, Canada

²Department of Civil & Environmental Engineering, Princeton University, Princeton, NJ 08544, USA

³Department of Materials Science and Engineering, University of California, Los Angeles, Los Angeles, CA 90024, USA

⁴Department of Civil Engineering, McGill University, Montréal, QC H3A 0C3, Canada

⁵Lead contact

*Correspondence: salmaan.craig@mcgill.ca
<https://doi.org/10.1016/j.xcpr.2023.101570>



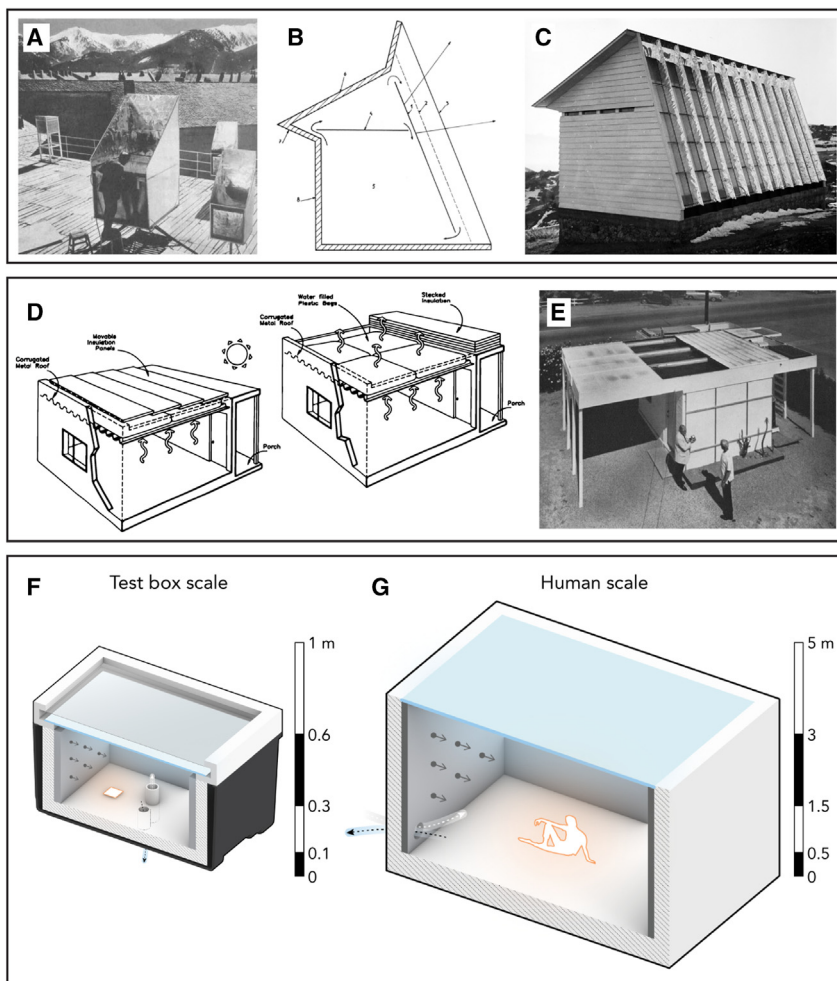


Figure 1. Passive radiative cooling in unventilated and ventilated enclosures

(A) View of an experimental cooling container used by Trombe and his team in Mont-Louis, France, undated.²³

(B) Diagrammatic vertical section of Trombe's patented design for the cold house, 1967.²⁴

(C) North-east view showing the radiative cooling facade of the cold house designed and built by Felix Trombe and his team in 1963–1963 in Odeillo, France.²⁵

(D) Schematic drawing of the Skytherm system during the day with the movable insulation covering the roof (left), and during the night with the water-filled bags exposed to the cold-infrared sky (right).²⁷

(E) Harold Hay and John I. Yellott in front of a prototype of the Skytherm system built in Phoenix, Arizona in 1967.²⁸

(F) Schematic of our test box, reproducing 1% of the thermal loads, losses, and air changes attributable to one occupant.

(G) Schematic of the proportions of the thermal mass, radiator, and ventilation openings needed for one occupant.

infrared-transparent plastic panels, with a spectrally selective radiator behind it, creating an air gap where air could circulate. The radiator produced cool air during the night, which descended into the room.²⁵ During the day, when the radiator overheated, the flow traps were closed, leaving the thermal mass inside the room to absorb excess heat. However, recent archival research shows that Trombe's lab assistants, who periodically inhabited his earlier solar test buildings, complained that opening windows was forbidden for thermal reasons.²⁵ If ventilation air changes threatened to nullify the

passive heating effects in these earlier solar house experiments, then it is likely that Trombe enforced the same closed-window policy in his cold house experiment, too. Otherwise, it would have been difficult to produce sub-ambient temperatures indoors, let alone maintain them.

Similarly, Harold Hay created the Skytherm system in the 1970s to combine night-time cooling and cold storage (Figures 1D and 1E).^{27,28,29} His design included a flat steel roof with water-filled plastic bags covered by movable insulation panels. At night, the insulation was removed, allowing the night sky to radiatively cool the roof's thermal mass. During the day, the insulation was put back in place to shield the water from the sun. The water bags could then cool the interior by thermal contact through the metal decking while ventilation was controlled by opening or closing windows. Hay's design was tested in several experimental buildings from 1975 to 1984 in the southwestern United States and successfully achieved sub-ambient cooling. Nonetheless, the commercialization of the Skytherm system was always hindered by its reliance on movable insulation, which demanded considerable work from the user and complicated mechanical components.

These historic experiments are valuable because they highlight the challenges of using terrestrial radiation to passively reject heat from inside buildings. Part of the challenge is minimizing counterproductive heat gains from the building envelope and maintaining healthy ventilation rates, even when air changes are a source of heating, making sub-ambient interior temperatures difficult to achieve. Inspired by Trombe and Hay's attempts, we explore a simpler passive cooling system with no mechanical equipment or moving parts. Our aim is to balance temperature-driven ventilation with thermal mass and sub-ambient cooling from an uninsulated roof. We choose to focus on the cooling performance in hot and dry climates, during periods of potential heat stress, or when it may be possible to obviate mechanical air-conditioning.

We begin by defining a reference case: an internal thermal mass with night ventilation, which is the current "gold standard" for passive cooling in hot and dry climates (assuming excavations for ground cooling are unfeasible and water is too precious to evaporate as a spray).^{30–34} The thermal mass, protected by external insulation, absorbs internal heat from people, devices, lighting, and so on during the day. The ventilation lets the mass discharge this heat at night. These air exchanges may be driven naturally through a combination of wind and buoyancy forces.^{35–37} We choose to utilize buoyancy forces for temperature-driven ventilation. In contrast, wind-driven ventilation is stochastic, making it harder to maintain regular air-changes and balance interior temperatures.

We then examine how to surpass this gold standard for passive cooling by adding 24-h radiative cooling from an uninsulated roof. We experimentally demonstrate a model enclosure that maintained an interior temperature of 3.9°C below the mean prevailing exterior temperature, and 8.9°C below the reference gold standard, while consistently venting nearly seven air changes per hour during the day. Our results show it is possible to cool interior spaces below their ambient temperature using passive radiative cooling and temperature-driven ventilation, ensuring adequate air changes from the exterior.

RESULTS

Heat balance

We define the evolution of the air temperature inside a ventilated enclosure as

$$\rho C p_{in} V_{in} \frac{dT_{in}}{dt} = W_V + W_M + W_R + W_E + W_H, \quad (\text{Equation 1})$$

where ρCp_{in} is the volumetric heat capacity of the air; V_{in} is the volume of interior air; W_V , W_M , and W_R are the internal heat exchanges with the ventilation, thermal mass, and the underside of the roof (i.e., soffit), respectively; W_E is the heat transfer through the insulated external walls; and W_H is the internal heat generated by people, devices, and so on.

Not only do we wish to put the interior space in radiant communication with outer space via the roof but we also want to put the interior air in fluid communication with the atmosphere. In the heat balance of [Equation 1](#), ventilation (W_V) heats or cools the interior depending on its sign (i.e., the relative temperature of the exterior). Ventilation is necessary for health reasons, as the COVID-19 pandemic has highlighted. We wish to understand how to achieve passive cooling to sub-ambient indoor temperatures without sacrificing healthy air changes. The geographical limits and practical applications may be evaluated once this physical balance is understood.

The driving force for buoyancy ventilation can be formulated as a reduced gravity, $g' = g\beta\Delta T$, where g is the gravitational acceleration, β is the coefficient of thermal expansion of air, and $\Delta T = T_a - T_{in}$ is the difference between ambient and indoor air temperature. The heat exchanges from the ventilation W_V is then calculated from the natural ventilation flow rate Q as

$$Q = A^* \sqrt{\frac{|\Delta pw - g'H|}{\rho}} \quad (\text{Equation 2})$$

$$W_V = \rho Cp_{in} \Delta T Q \quad (\text{Equation 3})$$

where A^* is the effective size of the ventilation openings, Δpw is the wind pressure difference between the openings, H is the height between the openings, and ρ is the air density. Wind and buoyancy forces may complement or compete with each other, depending on the vent locations and their orientation to the wind. Later, we design the vents to eliminate the influence of wind. In any case, we model the internal thermal mass as lumped (that is, neglecting the diffusion of heat through the mass) to simplify the thermal coupling with buoyancy ventilation

$$\rho Cp_M V_M \frac{dT_M}{dt} = -W_M \quad (\text{Equation 4})$$

$$W_M = S_M h_M (T_M - T_{in}), \quad (\text{Equation 5})$$

where T_M is the mass temperature, ρCp_M is the heat capacity of the thermal mass, V_M is the thermal mass volume, S_M is the surface area in contact with the indoor air, and h_M the heat transfer coefficient to and from the surface of the thermal mass in contact with the interior air. We also model the thermal mass in the roof radiator as a lumped mass

$$\rho Cp_R V_R \frac{dT_R}{dt} = W_{sky} - W_R \quad (\text{Equation 6})$$

$$W_R = S_R h_R (T_R - T_{in}) \quad (\text{Equation 7})$$

where the subscript R indicates the equivalent parameters for the radiator as for the thermal mass in [Equations 4](#) and [5](#), and W_{sky} is the balance of thermal radiation, solar radiation, and convection on the top surface of the radiator, defined below. We now report our experiment, investigating the coupling of thermal mass, buoyancy ventilation, and radiative cooling in passive building design. We show how to maintain

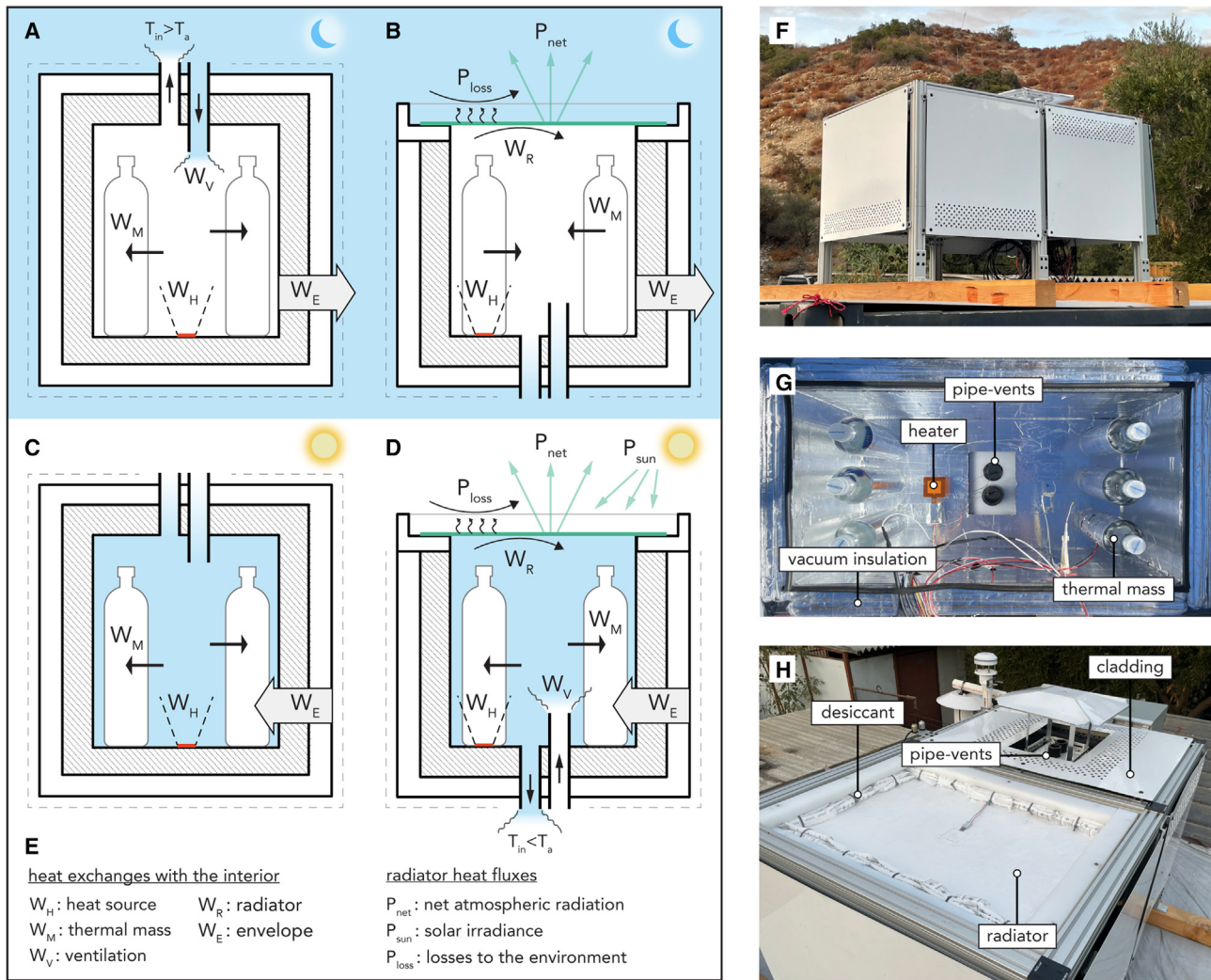


Figure 2. Experimental setup

(A) Reference box at night. Upwelling mixing ventilation occurs at night because the interior (T_{in}) is warmer than the exterior (T_a), and the ventilation stacks are positioned at the top of the box. The night ventilation lets the thermal mass discharge the heat accumulated during the day.

(B) Test box at night. There is no ventilation at night since the ventilation stacks are positioned at the bottom of the box and the interior is warmer than the exterior. Only the roof is responsible for cooling the interior air during the night.

(C) Reference box during the day. There is no ventilation during the day since the ventilation stacks are positioned at the top of the box and the interior is cooler than the exterior.

(D) Test box during the day. Downwelling mixing ventilation occurs during the day because the interior (T_{in}) is cooler than the exterior (T_a), and the ventilation stacks are positioned at the bottom of the box.

(E) Nomenclature.

(F) Photo of the experiment setup in Topanga Valley, California.

(G) Annotated photo showing inside the test box.

(H) Annotated photo showing the radiator on top of the test box (front) and the high-level pipe vents of the reference box (back).

sub-ambient interior temperatures while producing steady air changes, with results that scale to per-person heat loads and fresh-air requirements.

Experimental design

We installed two insulated boxes in a warm, dry climate (Topanga Valley, CA) with an open view of the sky (Figure 2). The first box, hereafter called the reference box, had an internal thermal mass, an internal heat source, and two upward-pointing

ventilation stacks (i.e., pipe vents). In this box, ventilation only occurred when the buoyancy pressure was negative (that is, when the interior temperature was warmer than the exterior), prompting upward flow through the shortest pipe vent (Figures 2A and 2C). The other box, hereafter called the test box, had the same thermal mass and internal heat source, but the roof was an uninsulated aluminum plate with a daytime radiative cooling material glued to its top surface (see section “[experimental procedures](#)”). The underside (soffit) of the radiator was directly coupled to the interior by natural convection. Its sky-facing side had an infrared-transparent guard above it to limit convective heating from the exterior. The wind guard was sealed and desiccants lined the edges of the radiator to eliminate surface condensation.

Our experiment uses temperature-driven ventilation in both the reference case and the test case. The reference case uses upwelling mixing ventilation to spontaneously cool the internal thermal mass at night (when $T_{in} > T_a$). The reference case therefore represents a gold standard for passive cooling, which the test case must outperform. In contrast, the test case uses downwelling mixing ventilation, which works only during the day (when $T_{in} < T_a$), so we could eliminate ventilation cooling effects at night and more clearly demonstrate the influence of radiative cooling in the experiment. As such, the ventilation of both boxes was driven by the temperature difference between inside and outside, but for opposite signs, biasing the reference box for night venting and the test box for day venting. In this way, both boxes could reach their lowest temperatures while still achieving the same average air changes over 24 h. In a real building, however, both ventilation approaches can be combined to produce continuous ventilation, switching between downwelling and upwelling by activating different vents as necessary.

We scaled the experiment targeting a flow rate of ~ 0.1 L/s, representing 1% of the ventilation rate that one person requires. (Engineering guidelines recommend 10 L/s per person in non-residential buildings, although these rates are likely to increase to 14 L/s following the COVID-19 pandemic.²²) Meanwhile, the differential height of the pipe vents helped to drive the buoyancy flow, promote good mixing of the interior air by the incoming plume, and ensure unidirectional flow through each pipe vent for measurement purposes.³⁷ The closeness of the pipes to each other, and the fact they hardly protruded outside the box (as shown in Figures 2A–2D) helped to eliminate differential wind pressure.^{31,38} Moreover, to ensure the scalability of our approach, we calculated the Rayleigh number $Ra = (g' Hb^3)/k \nu$ and the Reynolds numbers $Re = (g^{1/2} Hb^{3/2})/\nu$ for both boxes, where g' is the reduced gravity, Hb is the height of the interior space, and k and ν are the diffusivity and kinematic viscosity of air. Assuming a 5°C temperature difference with the exterior, the boxes achieve $Ra \approx 1.4 \times 10^7$ and $Re \approx 4,500$. These values confirm that the ventilation flows in the experiment are turbulent, replicating the advection-dominated heat transfer in full-scale buildings with buoyancy flow.

The thermal mass inside each test box was a set of water bottles, chosen for cost, simplicity, and volumetric heat capacity. The thermal mass, ventilation flow rate, and roof radiator were sized so that all the heat exchanges with the interior (listed in [Equation 1](#)) were reduced by the same order of magnitude, representing approximately 1% of the heat load and ventilation requirements typically associated with one occupant. Since ventilation exchanges were potentially the most challenging to get right, we started with [Equation 2](#), sizing the cross-sectional area and length of the pipe vents to achieve a flow rate of ~ 0.1 L/s (the equivalent of 10 L/s at building scale), assuming no wind and a 5°C temperature difference with the exterior.

Then, we calculated the radiative cooling roof area (S_R) needed to offset an internal heat source of 1.2 W (or 120 W) based on simulations for W_{sky} and the properties of the daytime radiative cooling material (described in section “[experimental procedures](#)”). In parallel, we used thermal mass scaling rules as a starting point to determine the surface area (S_M) and volume (V_M) of internal mass that would be needed to keep the interior temperature within a $\sim 5^\circ\text{C}$ range under an exterior temperature swing of $\sim 15^\circ\text{C}$.³² Finally, we input those values into our theoretical model (Equations 1–7) and proceeded by iteration to find the combination that would be both practical and produce the coldest and most stable interior temperature.

Temperature and flow rate

We ran two experiments under clear sky conditions and measured the air temperature and ventilation exchanges inside the boxes, as well as the other heat exchanges expressed in [Equation 1](#). During the first experiment in September, the interior temperature of the reference box fluctuated $4.3^\circ\text{C} \pm 2.5^\circ\text{C}$ above the mean prevailing ambient temperature T_{pm} ([Figure 3A](#)). (Note that the error reported here represents the difference between the mean daily maximum and minimum temperatures.) In comparison, the test box remained $1.6^\circ\text{C} \pm 6.8^\circ\text{C}$ below T_{pm} ([Figure 3A](#)). The interior temperature of the test box was less stable than the reference box, and its peak temperature occasionally exceeded that of the control, so we decided to add 1.5 times more thermal mass in the boxes to further stabilize their interior temperature in a second experiment. This took place in November, and the interior of the reference box fluctuated $5.0^\circ\text{C} \pm 1.7^\circ\text{C}$ above T_{pm} while the extra mass helped dampen the interior temperature swing ($T_{in,max} - T_{in,min}$) by factor 0.86 relative to the exterior. The test box varied on average $3.9^\circ\text{C} \pm 4.8^\circ\text{C}$ below T_{pm} and reduced the ambient temperature swing ($T_{a,max} - T_{a,min}$) by a factor of 0.59 ([Figure 3B](#)). The relative instability of the test box was caused by the variation in the radiator temperature since the test box had the same amount of internal thermal mass as the reference box.

The ventilation stacks in both boxes were designed to produce unidirectional, wind-insensitive ventilation and well-mixed thermal conditions inside the boxes (see section “[experimental procedures](#)”). We measured the flow velocity in each of the four stacks and used these measurements to derive a flow rate while validating [Equation 2](#). As intended, the ventilation did occur over half-day cycles based on the temperature difference between the inside and outside ([Figures 3C and 3F](#)). In September, the reference box vented on average $0.133 \pm 0.015 \text{ L/s}$ during the day, and the test box vented $0.061 \pm 0.013 \text{ L/s}$ during the night. (Note that the error reported here represents the reading error from the sensors, which was greater than the standard deviation.) In comparison, the reference box vented $0.143 \pm 0.015 \text{ L/s}$ during the day and the test box vented $0.115 \pm 0.014 \text{ L/s}$ during the night in November. Since the air temperature was more stable inside the reference box, it led to a bigger temperature difference with the outside and larger ventilation flow rates. Similarly, the temperature variations in the reference and test boxes were dampened by the additional thermal mass in November and therefore produced more ventilation.

Interior heat balance

Along with the temperature and ventilation flow measurements, we measured all the components of the heat balance in [Equation 1](#) (see section “[experimental procedures](#)”). In the reference box, the internal thermal mass produced alternating heating and cooling cycles (W_M), depending on whether it was warmer or cooler than the interior ([Figure 3D](#)). Because the ventilation only occurred when the inside

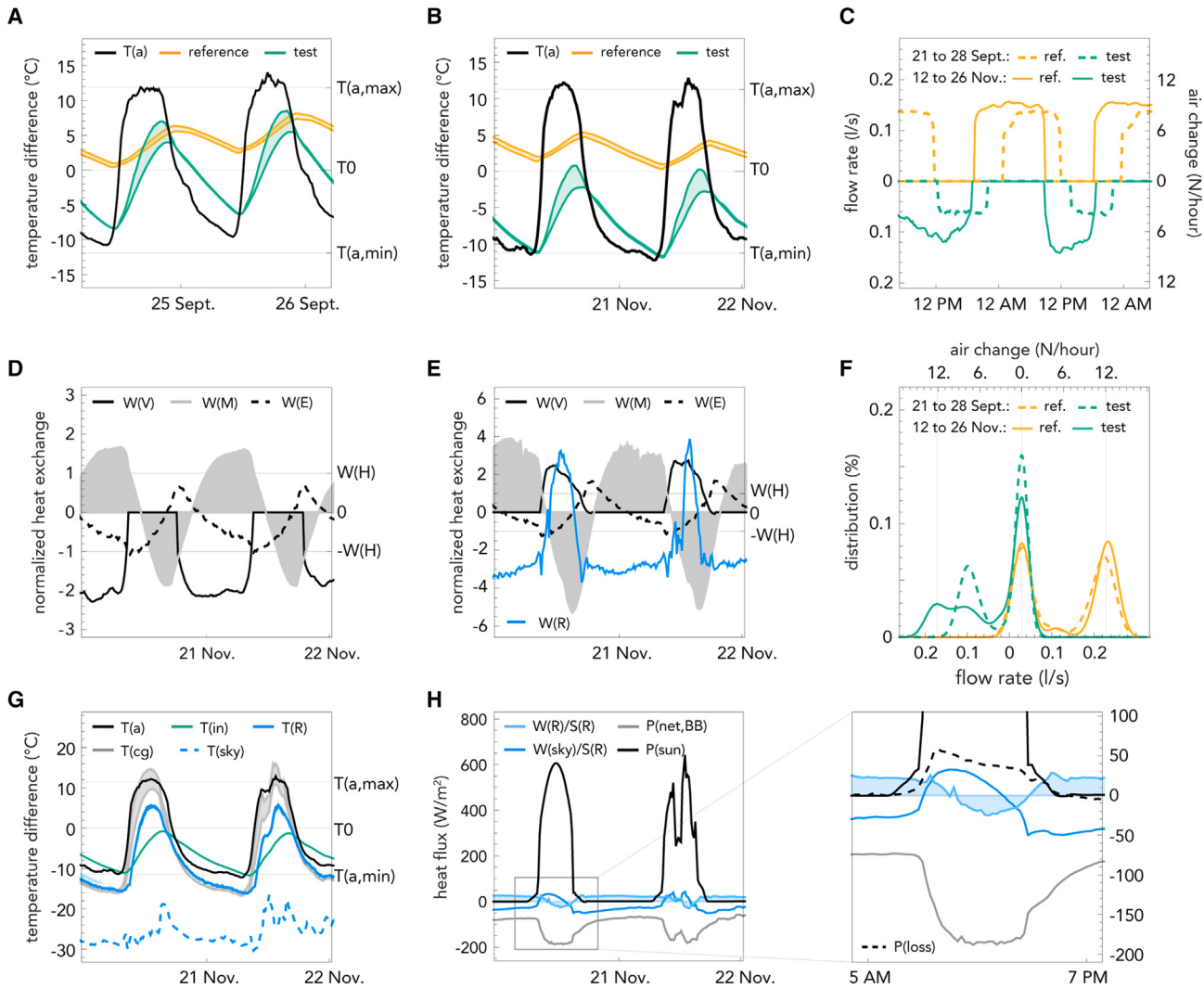


Figure 3. Temperature, ventilation flow, and heat exchange measurements

- (A) Air temperature T_{in} inside the reference (yellow) and test (green) boxes with ambient temperature T_a (black) for two typical days in September 2022 relative to the mean ambient temperature $T_0 = (T_{a,max} - T_{a,min})/2$. During that period, the mean prevailing ambient temperature T_{pm} was 21.9°C, with an average of 23.7°C between the daily maximum and minimum T_a .
- (B) Typical variations of T_{in} and T_a relative to the mean ambient temperature T_0 for 2 days in November 2022, after 1.5 times more thermal mass was added in both boxes. T_{pm} was 9.4°C, and the difference between the daily maximum and minimum T_a was 22.4°C. The interior of the reference and test boxes varied on average $5.0^\circ\text{C} \pm 1.7^\circ\text{C}$ above and $3.9^\circ\text{C} \pm 4.8^\circ\text{C}$ below the ambient, respectively.
- (C) Comparison of the ventilation flow rate Q and the number of air changes per hour in the reference and test boxes for two typical days in September (dashed) and November (solid) 2022. Since T_{in} is more stable in November, the temperature difference between T_a and T_{in} increases, and so does the ventilation rate.
- (D) Normalized heat exchanges through ventilation (W_V , solid black), with the thermal mass (W_M , gray) and through the envelope (W_E , dashed black) in the reference box during two typical days in November 2022 (scaled to $W_H = 1.2 \text{ W}$).
- (E) Normalized heat exchanges through the ventilation (W_V , solid black), with the thermal mass (W_M , gray), through the envelope (W_E , dashed black), and from the radiator soffit (W_R , blue) in the test box during 2 days in November 2022 (scaled to $W_H = 1.2 \text{ W}$). Note the change in the y axis scale.
- (F) Comparison of the distribution of the ventilation flow rate Q and the number of air changes per hour during the 7-day and 14-day experiments in September and November 2022.
- (G) Radiator temperature (T_R , solid blue) with the ambient air temperature (T_a , black), indoor air temperature (T_{in} , green), air temperature inside the convection guard (T_{cg} , gray), and effective sky temperature (T_{sky} , dashed blue) for two typical days in November 2022 relative to the mean ambient temperature T_0 .
- (H) Measured heat fluxes on the top surface (W_{sky}/S_R , blue) and soffit (W_R/S_R , light blue) of the radiator, with downward solar radiation flux (P_{sun} , solid black), net atmospheric radiation flux for a blackbody at ambient temperature ($P_{net,BB}$, gray), and predicted parasitic losses through the convection guard (P_{loss} , dashed black) for two typical days in November 2022 and from 5 a.m. to 7 p.m. on November 20.

of the box was warmer than the ambient air, the thermal mass cooled down at night faster than it warmed up during the day, biasing the system toward cooler temperatures.

In the test box, the heat absorbed by the thermal mass from ventilation changes during the day was discharged by the radiator at night through a combination of convection and radiation, or just radiation, depending on the temperature of the radiator. However, the roof thermal mass did overheat ($W_R > 0$) in the afternoon when the solar loads were particularly strong and when the interior temperature was at its coolest relative to the ambient (Figure 3E). At these times, the internal thermal mass (W_M) absorbed most of the heat brought in by ventilation, and the thermal inertia of the indoor air cooled the roof (W_R), not the other way around.

Radiator fluxes

At night, when the radiator is above ambient temperature, the radiator cools by a combination of terrestrial radiation and conduction/convection from the wind guard. However, when the radiator cools below the ambient temperature, terrestrial radiation is the only source of cooling. The radiator in our experiment was consistently below the ambient temperature at night, indicating that terrestrial radiation was the dominant source of cooling. Nevertheless, it is useful to separate the effects of different roof cooling phenomena in the data. We did so by simulating a case with a low-emissivity roof (see section “[impact of radiative cooling](#)” in “[experimental procedures](#)”). This simulated counter-example showed that, in our experiment, terrestrial radiation boosted the net cooling by an average of 8.7 W/m² per day, producing an interior temperature that was on average 4.8°C cooler than a case with a low-emissivity roof. Another important cooling effect to isolate is nighttime ventilation cooling, which is why we designed our test box to ventilate only during the day, when the interior was warmer than the exterior. The ventilation flow measurements show that the air exchanges stopped during the night, as planned. Finally, we were also able to verify that the desiccants under the wind guard worked as planned, stopping condensation occurring on the radiator on humid nights, so we could neglect latent heat exchange effects from the energy balance (see section “[latent heat phenomena](#)” in “[experimental procedures](#)”).

The interior cooling power of the radiator (i.e., from the soffit) was on average 1.9 times more than the heating power from the heat source. However, the cooling effect from the soffit was not consistent over 24 h (Figure 3E). As a result, the internal thermal mass would cool down at night faster in the test box than in the reference box, but it also warmed up faster during the day, so the stabilizing effect of the thermal mass was limited. In this regard, it is important to understand how to potentially stabilize the roof temperature, which is not obvious with conjugate heat exchanges occurring simultaneously on both sides (Equation 6). The balance of the radiation and convection fluxes at the top surface of the radiator (W_{sky}) may be calculated from the effective sky temperature T_{sky} as

$$T_{sky} = (T_a^4 - P_{net,BB}\sigma^{-1})^{1/4} \quad (\text{Equation 8})$$

$$W_{sky} = S_R (\epsilon \sigma (T_R^4 - T_{sky}^4) - \alpha P_{sun} - P_{loss}), \quad (\text{Equation 9})$$

where ϵ is the hemispherical emissivity of the roof surface (see section “[experimental procedures](#)”), $P_{net,BB}$ is the net atmospheric radiation flux for a blackbody at ambient temperature, S_R is the surface area of the radiator, αP_{sun} is the absorbed solar radiation flux based on the surface’s solar absorptivity α (see section “[experimental](#)

procedures”), and P_{loss} is the sum of parasitic losses to the environment, including convection and re-radiation from the convection guard.^{16,39}

In the November experiment, the radiator temperature (T_R) followed the ambient temperature (T_a) but remained on average 6.4°C and 3.7°C cooler under peak solar irradiance and during the night, respectively (Figure 3G). Even though T_R stayed below the ambient temperature throughout the experiment, it followed the ambient temperature closely, causing it to overshoot the indoor air by up to 9.5°C in the afternoon. This instability was not helped by overheating inside the convection guard ($T_{cg} > T_a$), which exceeded the ambient temperature by up to 4°C in the afternoon, adding unnecessary heat to the radiator (see P_{loss} in Figure 3H).

Interior temperature stability

To further analyze the sub-ambient temperatures inside the experiment boxes and understand if they could have evolved with more stability, it is useful to normalize the interior temperature as

$$\theta = \frac{(T - T_0)}{\Delta T_a}, \quad (\text{Equation 10})$$

where $T_0 = (T_{a,max} + T_{a,min})/2$ is the daily mean ambient temperature and $\Delta T_a = |T_{a,max} - T_0|$ is the daily ambient temperature increment above the mean. In Figure 4, we compare these temperatures with the prevailing mean ambient temperature, which serves as a reference in the ASHRAE (American Society of Heating, Refrigerating and Air-Conditioning Engineers) adaptive comfort standard for naturally ventilated buildings.⁴⁰ This design standard reflects empirical evidence that peoples' thermal expectations change with the predominant weather and allows a 5°C–7°C range of acceptable indoor temperatures.^{41,42} The upper and lower limits to keep at least 80% of the occupants comfortable are

$$T_{op,min} = 14.3 + 0.31 T_{pm} \quad (\text{Equation 11})$$

$$T_{op,max} = 21.3 + 0.31 T_{pm} \quad (\text{Equation 12})$$

where T_{op} is the indoor operative temperature (a composite of the radiant and air temperature) and T_{pm} is the prevailing mean ambient temperature (defined as the average of the daily mean outdoor temperature for a sequence of 7–30 days).⁴⁰ It is worth noting that, in the range $20.7^\circ\text{C} < T_{pm} < 30.9^\circ\text{C}$, an interior temperature equal to the prevailing mean is comfortable. Above this threshold ($T_{pm} > 30.9^\circ\text{C}$), the interior space needs to be cooled below the prevailing mean, working against daytime ventilation (W_V), which will act as a heat gain.

As Figure 4A shows, the mean temperature in the test box stayed below the prevailing mean (θ_{pm}) for the 14 days during the November experiment, while the reference box stayed above this threshold. (Note that, while T_{pm} is a constant, θ_{pm} varies slightly day to day in Figures 4A and 4B because it is normalized for daily values of T_0 and ΔT_a .) For reference, the scale 0–1 represents a temperature difference of $11.4^\circ\text{C} \pm 1^\circ\text{C}$, where the reported error is the standard deviation between daily values of ΔT_a .

With these normalized temperatures, we can see what the performance might be like in a similar climate during a hot period ($T_{pm} > 30.9^\circ\text{C}$), relative to the prevailing mean and the current gold standard (thermal mass and night ventilation). While the consistent sub-ambient temperatures are promising, their variability day and night could cause discomfort (Figure 4A).

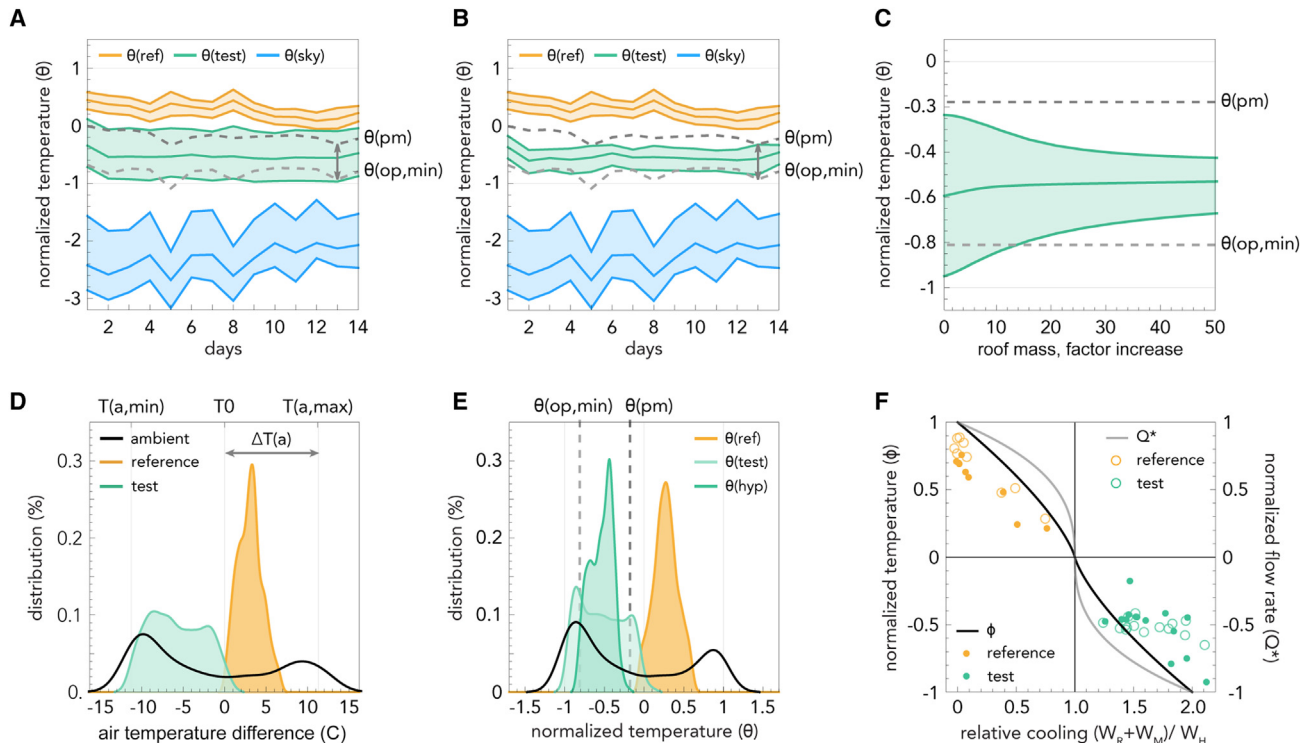


Figure 4. Interior temperature stability and prediction for a massive roof radiator

(A) Daily minimum, maximum, and mean temperatures inside the reference (θ_{ref} , yellow) and test box (θ_{test} , green), with the effective sky temperature (θ_{sky} , blue, Equation 8) from November 12 to 26 2022. All temperatures are normalized relative to the ambient temperature using Equation 10. The width of each band indicates the daily maximum and minimum temperatures. The two dashed gray lines are the prevailing mean ambient temperature θ_{pm} , and the normalized lower limit for adaptive comfort $\theta_{op,min}$ when $T_{pm} = 30.9^\circ\text{C}$ and $\theta_{pm} = \theta_{op,max}$.

(B) Predictions from our calibrated model showing the hypothetical interior temperature of the test box (θ_{hyp} , green) with a 20-fold increase in the roof's thermal mass.

(C) Influence of the roof's mass increase on the daily minimum, maximum, and mean temperatures inside the test box.

(D) Distribution of T_{in} and T_a from November 12 to 26, 2022 for the reference (yellow) and test (green) boxes relative to the mean ambient temperature $T_0 = (T_{a,max} - T_{a,min})/2$.

(E) Distribution of the normalized temperature inside the reference (yellow) and test (light green) boxes with ambient temperature (θ_a , black) and the hypothetical scenario with more thermal mass in the roof (θ_{hyp} , green).

(F) Influence of the relative cooling ($W_R + W_M$)/ W_H on the daily mean temperature and ventilation flow rate inside the reference (yellow) and test (green) boxes. The normalizations are defined in text.

One way to improve the indoor temperature stability is to add more thermal mass to the roof, which we explored theoretically after calibrating our model (Equations 1 to 7) to the experimental data (for reference, an illustration of what the roof and architecture might look like is shown in Figure 5.) We achieved this calibration by finding the heat transfer rates on the surface of the internal thermal mass that minimized the error between W_M measured and predicted from Equation 5 (Figure 6E). We defined that error as the root-mean-square error (RMSE):

$$RMSE = \sqrt{\frac{\sum_{t=1}^T (P_{meas,t} - P_{pred,t})^2}{T}} \quad (\text{Equation 13})$$

where T is the duration of the experiment and $P_{meas,t}$ and $P_{pred,t}$ are the measurements and predictions at time t during the experiment. We repeated the same process for W_R on the radiator soffit, but with two convection rates, one for the period during the day when $T_R > T_a$, and one for the night when $T_a > T_R$, to account for the different modes of surface convection (Figure 6F). For W_{sky} on the sky-facing surface

of the radiator, we found the effective heat transfer rate for $P_{loss} = h(T_a - T_R)$ that would minimize the error between W_{sky} measured and predicted from [Equation 9](#) with on-site measurements of P_{sun} and $P_{net,BB}$ ([Figure 6F](#)). In this case, calibrating P_{loss} for two heat transfer coefficients to capture two convection regimes day and night did not improve the fit between the predictions and the measurements, since T_R remained sub-ambient throughout the experiment. Furthermore, for simplicity, we assumed P_{loss} to be a function of T_a (instead of T_{cg}).

In [Figure 4B](#), we used our calibrated model to predict the temperature inside the test box, assuming the roof radiator was 20 times thicker and therefore had 20 times more thermal mass ($\rho C p_R V_R$). In this scenario, the aluminum sheet would increase from 6 to 120 mm. This extra mass stabilizes the roof temperature around a daily mean which, in turn, stabilizes the convective heat exchanges with the interior (W_R). For reference, a concrete roof that is 129 (± 22) mm thick, where the uncertainty depends on the thermal properties, would have the same volumetric heat capacity per unit area.⁴³ As shown in [Figure 4C](#), the amount of thermal mass in the roof can be tuned for different objectives. The mean interior temperature does not significantly vary after a 6-fold mass increase, and there are diminishing returns with interior temperature stability after a 20-fold mass increase. These results help evaluate the cooling potential of additional roof thermal mass alongside broader architectural considerations, such as the roof's structural performance and its embodied carbon footprint.

In [Figure 4E](#), we compare the distribution of the normalized temperature for the test radiator (light green) and the hypothetical radiator with more mass (green). The latter is stable enough to remain within the range of adaptive comfort while also staying below the prevailing mean ambient temperature. As such, [Figure 4E](#) suggests that stable, sub-ambient cooling is possible below the prevailing mean. In dry climates, this can be useful for maintaining comfort in hot periods ($T_{pm} < 32^\circ\text{C}$) according to international standards for adaptive thermal comfort in naturally ventilated buildings.⁴⁰ Note that the prevailing mean (T_{pm}) is not the same as the peak exterior temperature on any given day. Therefore, this approach could still work as peak exterior temperatures approach 37°C , so long as the night temperatures are sufficiently cool. In cases where the prevailing mean or peak exterior temperatures are too high to stay within the adaptive comfort threshold, this approach could still produce interior temperatures that are cooler and, therefore, safer during dangerous heat waves. In these extreme cases, ventilation rates could be reduced to maintain cooler temperatures.

Seasonal adaptation

In [Figure 4F](#) we consider the influence of the relative cooling W_C/W_H on the daily mean temperature and ventilation flow rate inside both boxes, following the scaling by Chenvidyakarn and Woods.^{35,44,45} The temperatures are normalized with $\varphi = (T_{in} - T_a)/\Delta T_0$ and the flow rates with $Q^* = Q/Q_0$ where ΔT_0 and Q_0 are the reference temperature excess and flow rate that would occur in steady state without any cooling. The reference flow rate Q_0 is calculated from ΔT_0 using [Equation 2](#), and ΔT_0 is found by solving for the balance $W_H = W_V + W_E$ where W_H is the constant 1.2 W heat input, W_V is the ventilation heat exchanges defined in [Equation 3](#), and $W_E = UA\Delta T$ is the steady-state envelope heat exchange. We calculated the two references curves φ (black) and Q^* (gray) by solving for ΔT with the balance $W_H - W_C = W_V + W_E$. The curves represent an idealized limit, assuming the internal heating and cooling fluxes are independent and the system has reached steady state. The measurements are daily averages and fall on one side of this limit. When plotting

the data, we set $W_C = W_M + W_R$ as the average daily cooling from the thermal mass (W_R , [Equation 5](#)) and the radiator (W_R , [Equation 7](#)). The upper left quadrant represents scenarios where heating dominates and the buoyancy forces promote upward flow. The lower right quadrant represents scenarios where cooling dominates and the buoyancy forces promote downward flow. This scaling is useful for two things. First, it is useful for initial design, before detailed simulation, to estimate the size of the radiator in relation to the internal heat loads, thermal mass, and ventilation rate. Second, it is useful for considering measures to switch between passive heating and cooling modes with the change of seasons, such as adjusting the vents to vary the ventilation rate, letting low-angle winter sunshine enter the building, or speculating on new technologies for adaptive insulation and switchable spectral properties.

DISCUSSION

Our experiment suggests it is possible to cool a naturally ventilated building below the prevailing ambient temperature using an uninsulated roof to passively reject heat to the sky and through the atmospheric window, day and night. We showed how to do this while maintaining steady air changes, using natural mixing ventilation, and how to harness these buoyancy forces in upward or downward flow, independent of wind effects. We compared the results with a reference box representing the current gold standard for passive cooling, which is an internal thermal mass with night ventilation. The test box was markedly cooler than the reference box, but the interior temperature was less stable. Therefore, to generalize the results, we used a calibrated model to show how adding thermal mass to the roof radiator could stabilize the temperature evolution of the interior air, resulting in a temperature range that is narrow like the gold standard but still well below the prevailing mean. International thermal comfort standards for naturally ventilated buildings define acceptable indoor temperature ranges relative to the prevailing mean. In hot periods, it is necessary to keep the interior below the prevailing mean, but it is difficult to do this by passive means alone, without sacrificing air changes. Our experiment suggests how to use radiative cooling in these situations to improve on the current gold standard for passive cooling, without sacrificing ventilation.

The design of our experiment makes it possible to scale the results to consider the dimensional implications for real buildings. To meet the cooling needs of one person, based on our test box, the surface area of internal thermal mass would be approximately 40 m^2 per person, assuming a heat storage capacity per unit area similar to that in the experiment, while the radiator surface would be approximately 16 m^2 per person ([Figure 5](#); [Table 1](#)). These calculations assume a ventilation rate ($W_V / \rho C p_{in} \Delta T$) of 10 L/s per person and an internal heat generation rate (W_H) of 120 W per person.

We also simplified our simulations by using constant, albeit calibrated, heat transfer coefficients, knowing that, in reality, they depend on how the temperature difference evolves (e.g., $h \propto \Delta T^{1/4}$ for natural convection^{46,47}) and that we had used infrared reflective tape to eliminate radiant heat transfer inside the box. It is important to bear these nuances in mind when scaling up, as the model is sensitive to the heat transfer coefficients (as indicated in [Figures 7E](#) and [5F](#)). For example, with natural convection on horizontal surfaces, both flow states, a quiescent boundary layer or entrainment from disorderly plumes, are self-similar with growing plate size.⁴⁶ However, on vertical surfaces, the height influences the transition to turbulence and, in a naturally ventilated enclosure, the entrainment from a “peeling-onion”

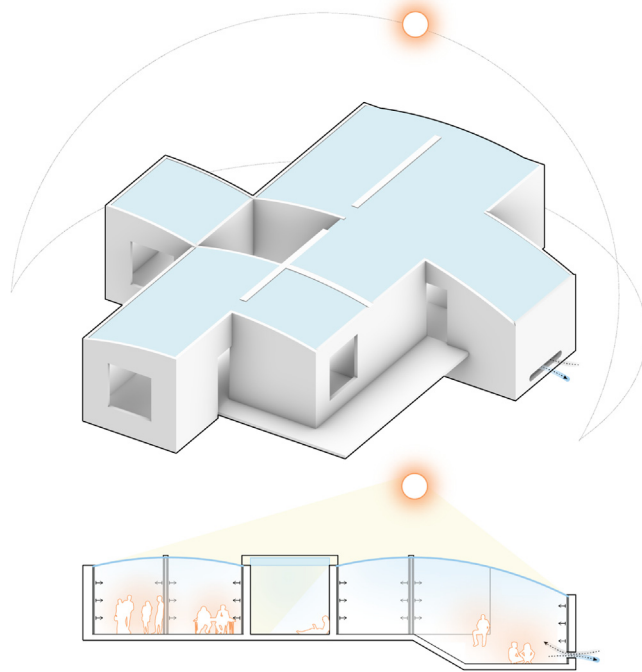


Figure 5. Schematic section and axonometric view of an architectural concept

The proportions of the internal thermal mass, radiator, and ventilation openings are based on [Table 1](#) and match the thermal loads, losses, and air changes required for 10 people. External wall insulation not shown.

boundary layer.⁴⁸ Comprehensive reviews of which surface heat transfer correlations to use for buildings in different scenarios are available in the literature.^{49–52}

One can consider substituting many kinds of thermal mass materials while scaling up. For example, the water bottles used as internal thermal mass could have been replaced by ~3-cm-thick concrete panels in the experiment, and we have assumed this thickness of concrete in our hypothetical scenarios for multiple occupants in [Figure 5](#). However, it is important to note that our model assumes a lumped thermal mass with a notional thickness expressing the ratio between the mass's volume and surface area in contact with the indoor air ($l_M = V_M/S_M$). This assumption is valid for sufficiently low Biot numbers, when the temperature gradients inside the mass are negligible. However, for thicker construction elements, such as concrete floor slabs, it is necessary to account for heat diffusion, which results in lower efficacy because isotherms take several hours to travel through the mass.³⁰ Likewise, the effective size of the ventilation openings A^* does not scale proportionally with the flow rate but rather depends on the height of the buoyancy column driving the ventilation and the pressure losses through the ventilation loop (see section “[experimental procedures](#)”).

The value of infrared-transparent convection guards in radiative cooling assemblies has been a sticking point in the literature thus far.⁵³ In theory, they should make the radiator more effective when it operates below ambient temperature, guarding against wind and promoting quiescence in the air gap for some insulating effect.

However, when the radiator is above ambient temperature, convection helps cool it, while any re-radiation from the guard will diminish the radiator’s ability to reject heat.

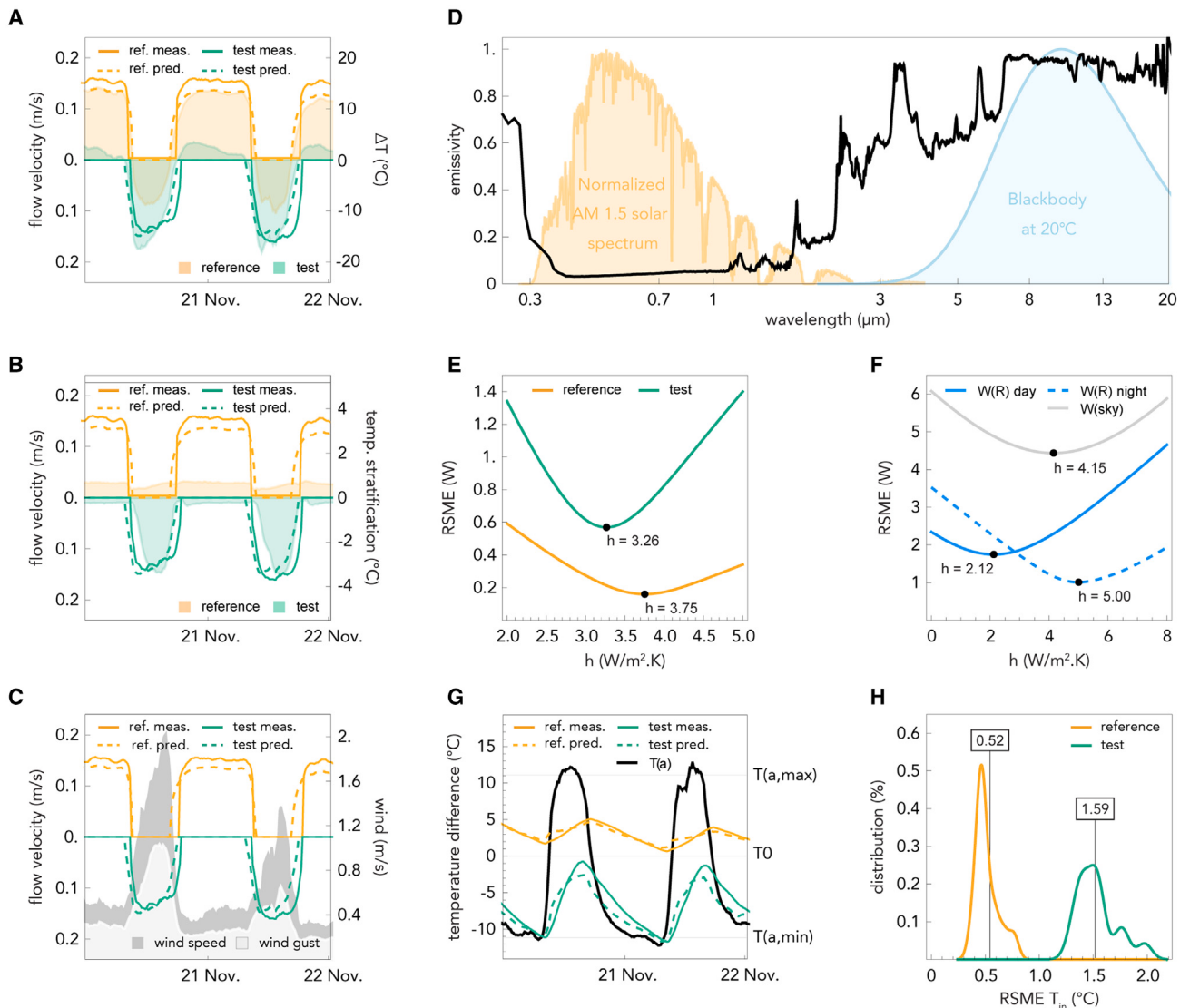


Figure 6. Performance characteristics and model calibration

- (A) Comparison of the flow velocity measured in the inflow pipe vents with the temperature difference between the ambient and the interior temperature ΔT . The pipe vents in the reference (yellow) were designed to ventilate only when $\Delta T > 0$. Inversely, the test box (green) was designed to ventilate only when $\Delta T < 0$.
- (B) Comparison of the flow velocity with the temperature stratification measured at 0.1 and 0.2 m inside the boxes. The pipe vents were designed to produce well-mixed indoor thermal conditions. The stratification in the test boxes was likely due to the radiator overheating during the day.
- (C) Comparison of the flow velocity with wind gust (m/s) and speed (m/s). Both sets of pipe vents were designed to be wind insensitive.
- (D) Wavelength-dependent emissivity of the radiative cooling material measured at near-normal incidence.
- (E) Calibration of the heat transfer coefficient on the internal thermal mass to minimize the error (RMSE) between W_M measured and predicted from Equation 5. RMSE is defined in Equation 13.
- (F) Calibration of the heat transfer coefficient on the soffit and top surface of the radiator to minimize the error between W_R and W_{sky} measured and predicted from Equations 7 and 9, respectively.
- (G) Comparison of the measured (solid) and predicted (dashed) T_{in} in the reference (yellow) and test (green) boxes for two typical days in November 2022.
- (H) Distribution of the daily RMSE for T_{in} in the reference (yellow) and test (green) boxes for the 14-day experiment in November 2022. In the test box, the predictions underestimated the measurements by 1.59°C on average, compared to 0.52°C in the reference box.

Table 1. Scaling up the critical dimensions of the test box

	1:100	1 person	10 people
Ventilation flow rate Q (L/s)	0.1	10	100
Buoyancy height H (m)	0.134	0.3	0.3
Effective vent. Area A^* (m ²)	0.001	0.035	0.35
Thermal mass thickness l_M (m)	0.03	0.03	0.03
Thermal mass surface S_M (m ²)	0.396	39.6	396
Radiator surface S_R (m ²)	0.155	15.5	155

Meanwhile, no one has yet produced a guard that combines infrared transparency with economy and durability for construction. So, are they necessary? Our measurements in the cavity suggest that the convection guard produced some unhelpful overheating in the daytime. This overheating could be attributed in part to the presence of solar-absorptive elements other than the radiator inside the convection guard, such as the desiccant bags, and might have been minimized by changing its design. The sub-ambient cooling performance may also have been improved by using a radiator with higher solar reflectance. For reference, our radiator had a solar reflectance of 93.8% (see section “[experimental procedures](#)”), whereas radiative cooling paints report a solar reflectance of 98%.⁶ This could lead to enough cooling where the convection guard helps during the day. In which case, adding a second layer of infrared-transparent film may help further. Nonetheless, our results suggest that convection guards may be an unnecessary complication with diminishing returns for this kind of real roof application, at least on sites where wind exposure is mild.

It would therefore be interesting to replicate the study without a convection guard and more thermal mass in the roof, at the amount we predict will stabilize the interior temperature. One effect that might influence the sky-facing heat balance in this scenario is dewfall powered by radiative cooling and then evaporation powered by sunshine.^{54,55} While late-night dewfall would add latent heat to the radiator, surface evaporation could help cool the radiator in the morning. Dewfall could also promote self-cleaning on a super-hydrophobic radiator, helping to maintain spectral efficiency over the building’s lifetime.^{56,57}

It is important to emphasize that this study is focused on hot, dry climates. Not only are skies colder and winters milder in these climates but indoor humidity is less of a concern, not just for thermal comfort and heat stress but for the risk of condensation forming on cool, interior surfaces, which, if moisture lingers, can lead to mold growth and serious respiratory health problems. Regular air changes are essential in this regard, and we have shown how to produce these naturally while balancing the interior temperature. Dehumidification may be necessary at times in the room, with the added benefit that it can be used to reduce the wet bulb temperature during dangerous heat stress events.^{58–60}

The idea of self-cooling, self-venting buildings, which are simple by design and straightforward to build, is attractive. However, it is important to recognize that there are limits to radiative cooling and that natural ventilation is not always possible or necessarily healthier than mechanical ventilation. Outdoor air dilutes contaminants with indoor sources but brings in outdoor contaminants that may be

hazardous, such as ozone and particulate matter. There is no reason our model cannot be applied with forced ventilation, allowing the air to be filtered. However, it is worth noting that virtually any air treatment method has both benefits and risks associated with it. Material collected on mechanical filters can interact with chemicals in the air to create secondary contaminants, and even germicidal light photochemistry can produce by-products.⁶¹ The industry lacks a comprehensive view of all these measures to help inform decisions about what should be used under what circumstances. However, one thing that is set to change in the aftermath of the COVID-19 pandemic is the recommended rates of outdoor air changes, which are likely to increase for every kind of building.²²

Removing insulation from a roof structure made from concrete, steel, or vaulted tiles may seem like a crude and counterintuitive proposition at first, but it could be relevant in hot and dry climates for a broad range of civic, commercial, and domestic spaces, such as market halls, community centers, low-rise condos with covered courtyards, and attic spaces that pre-cool fresh air. It can also be applied, for example, to community sports halls and cooling centers in towns and cities suffering from dangerous heat waves to provide respite, especially during power shortages when mechanical air-conditioning is not available. More generally, our work points to the need to re-examine basic assumptions on building insulation when accounting for new material capabilities that alter the flows of radiant heat between the building and its environment. There are no universal solutions to sustainable cooling, so we must also challenge universal ideas of thermal comfort.⁶² The infrastructure needed to produce constant and narrow temperature ranges, in every room, all the time, is not a pattern that can be thoughtlessly replicated. If the climate is very hot, hybrid approaches are also possible, where some rooms are climate controlled (and therefore need full insulation), while adjacent spaces make use of passive cooling measures, old or new.⁶³ In these buildings, where spaces follow a thermal hierarchy,⁶⁴ the aim of passive cooling may not be comfort *per se* but guaranteeing better or safer conditions than outdoors as part of a diverse range of indoor thermal environments.^{65,66} This can work knowing that, in very hot weather, occupants can adapt by changing what they are doing or moving to a different room.⁴² The design of built infrastructure determines whether cooling technologies can operate efficiently. However, skillful passive design can also influence behavior more broadly, helping to reduce temperature demand, nudge thermal expectations, leverage cultural adaptations to heat, and save lives when extreme heat coincides with blackouts.^{2,41,62}

EXPERIMENTAL PROCEDURES

Resource availability

Lead contact

Further information and requests for resources should be directed to and will be fulfilled by the lead contact, Salmaan Craig (salmaan.craig@mcgill.ca).

Materials availability

This study did not generate new unique materials.

Data and code availability

All original data and code have been deposited at Zenodo: <https://doi.org/10.5281/zenodo.8164886>. Background Oriented Schlieren flow visualizations, illustrating the architectural concept in action, are also included in this dataset. Any additional information required to reanalyze the data reported in this paper is available from the lead contact upon request.

Installation and box design

The test boxes were installed on a T-slotted aluminum frame, which lifted them 0.34 m above the roof of the shipping container in Topanga Valley, California (34.118063, -118.579955). The container was covered with a light-colored tarpaulin to limit heat radiation to the bottom of the boxes. White polyvinylidene fluoride (PVDF)-coated aluminum sheets were mounted on the T-slotted aluminum frame as cladding to protect the boxes from sun exposure. The cladding was partially perforated and did not touch the boxes to create a ventilated cavity, so the outer surface of the boxes would not exceed ambient temperature. Sensors were mounted on the frame next to the boxes to measure wind (Atmos 22 anemometer), air temperature and relative humidity (Apogee EE08-SS with an aspirated radiation shield), ambient pressure (Apogee SB-100), and incoming long- and shortwave radiation (Apogee SL-510-SS and SP-510-SS).

The interior space inside each box consisted of an airtight $0.3 \times 0.6 \times 0.3$ -m enclosure made of 2-mm-thick thermoplastic polyester (PETG). The inside of the enclosure was lined with aluminum foil tape to limit radiative heat exchanges. The outside was covered with two layers of 24-mm vacuum-insulated panels (Panasonic U-Vacua Series VIPs) with a total U value of $0.04 \text{ W/m}^2\text{.K}$ to minimize heat transfer through the envelope (W_E). The enclosure was installed inside a $0.53 \times 0.76 \times 0.45$ -m waterproof case (Pelican iM3075 Storm Transport Case). The space between the case and the VIPs panel was filled with ~ 30 -mm-thick polyurethane ether foam. A heat flux and surface temperature sensor (Huskeflux FHF04) was mounted at mid-height on one of the interior walls, and two thermistors (Apogee ST-100) measured air temperature at 0.1 and 0.2 m inside the enclosure. The internal heat source in each box was a self-calibrating heat flux sensor with an integrated 1.2-W heater (Huskeflux FHF04SC). The thermal mass in each box was 4×1 -L water bottles (Smartwater) wrapped in aluminum foil tape for the September experiment, and we added two additional bottles in each box before the November experiment. The total surface area of the water bottles in thermal contact with the interior air was 0.26 and 0.40 m^2 for the September and November experiments, respectively. A heat flux and surface temperature sensor (Huskeflux FHF04) was mounted at mid-height on one of the bottles in each box.

Ventilation design

The ventilation stacks were two PVC pipes with 39-mm interior diameter, 0.2 and 0.13 m long, respectively. The short stack was the outflow vent and was mounted flush with the PETG enclosure. The long stack was the inflow vent and protruded 0.66 mm inside the PETG enclosure. The buoyancy column driving the ventilation (H in [Equation 2](#)) was 0.13 m and corresponds to the height difference between the bottom of the inflow vent and the top of the outflow vent. Chimney caps protected both sets of stacks from rain and radiation from the surroundings. Sensors were measuring air temperature and wind velocity midway in each of the four stacks at the center of their cross section. We derived the flow rate (Q) from the flow velocity (u) as $Q = A^* u$, with $A^* = cd A$ where A is the cross-sectional area of the pipe vent and c_d is the discharge coefficient accounting for the loss in pressure across the ventilation loop. We estimated the latter with $c_d = \sqrt{\sum_i \zeta_i}$ where ζ_i are coefficients for the friction resistance and local pressure losses at the entrance and exit of each vent pipes.⁶⁷ The discharge coefficients c_d are 0.49, and 0.47 for the reference and test boxes, respectively. The associated A^* were used with [Equations 2](#) and [3](#) to predict the flow rate (Q) and ventilation heat transfer (W_V) from the temperature difference between the interior and exterior in the calibrated model. In [Figures 6A–6C](#), those predictions are shown to be in good agreement with the measurements.

We designed our pipe vents to have similar effects on the interior as buoyancy-driven mixing ventilation but with unidirectional flow in the ventilation stacks. Typically, mixing ventilation entails using a single opening as both inlet and outlet, causing the air entering the room to instantaneously mix with the outgoing air.^{35,36} This approach produces uniform indoor air temperature and is inherently sign dependent, but it also complicates the measurement of flow rate because of turbulence in the vents and creates significant pressure losses. With two ventilation stacks, the test box still produced sign-dependent ventilation because the interior air could only escape through the pipe vents at the bottom of the box when it was denser (or cooler) than the ambient air. During the day, negative buoyancy pressure drove warm air out of the short stack while sucking cold ambient air through the long stack. The same occurred in the reference but for the opposite temperature sign since the pipe vents were at the top of the box (Figure 6A).

For the ventilation to produce uniform indoor air temperature, we adjusted the length of the long pipe vent protruding inside the test box so it would end below the level at which the indoor air would naturally stratify. As such, we expected the plume of incoming warm exterior air to entrain some of the cold air from the stratified layer up and therefore help to maintain well-mixed thermal conditions inside.³⁷ As shown in Figure 6B, this strategy was more successful in the reference box, where the temperature difference between the top and bottom of the enclosure remained under 1°C. In the test box, the temperature stratification reached up to 3°C when the ventilation was flowing, but we believe this might have been amplified by overheating of the radiator soffit in the afternoon. Last, for the ventilation to remain primarily driven by thermal buoyancy and less sensitive to wind, we installed the two pipe vents close to one another, with their exterior end almost flush with the waterproof case. Since the wind pressure difference between the two openings was minimal, the ventilation flow was unaffected by wind speed changes or gusts during the experiment (Figure 6C).

Radiator design

The sky radiator was a low-cost multilayered daytime radiative cooling material spray glued on a 6-mm-thick 0.46 × 0.69-m aluminum plate. The material was a porous polyethene-based white material with a thermally emissive fluoropolymer film bonded to it. The wavelength-dependent absorptivity/emissivity of the radiator is shown in Figure 6D. The spectral properties were measured with Perkin Elmar Lambda 950 UV-Vis-NIR spectrophotometer with an integrating sphere module for the 0.2- to 1.5-μm range. A Bruker Invenio R Fourier transform infrared (FTIR) spectrophotometer with an integrating sphere and MCT (Mercury-Cadmium-Telluride) detector from IR Associates was used for the rest of the wavelengths up to 20 μm. We assumed $\epsilon = 0.90$ for the rest of the spectrum, since fluoropolymers are emissive in that range. All the measurements were done with light at near-normal incidence, or almost perpendicular to the surface. The actual solar reflectance and thermal emittance of the radiator could therefore be slightly higher in the shortwave range and slightly higher in the longwave range if all angles of incidence were accounted for. To model the heat fluxes at the top surface of the radiator, we calculated the solar absorptivity $\alpha = 0.062$ (0.3–2.5 μm) based on the AM 1.5 Global solar spectrum, and the emissivity $\epsilon = 0.916$ (5–20 μm) based on the spectral intensity emitted by a blackbody at 20°C (Figure 6D).

The radiator plate was mounted inside an acrylic module and rested on top of the PETG enclosure. An infrared-transparent polyethylene (PE) film (~20 μm thick, with an estimated average transmissivity of ~85%) was stretched 35 mm above the radiator plate. The underside of the radiator was directly exposed to the interior, with a surface area of 0.2 m². This soffit was covered with aluminum foil tape like the

rest of the PETG enclosure to limit radiative heat exchange between internal surfaces. A heat flux and surface temperature sensor was mounted at the center point on both sides of the radiator aluminum plate (under the radiative cooling material and under the aluminum foil tape).

Impact of radiative cooling

We used our calibrated model to quantify the relative impact of radiative cooling on the interior temperature evolution. We considered a simulated case similar to the test box, but with an uninsulated roof that has a thermal emissivity (ϵ) of 10% such that the effect of radiative cooling was negligible. As shown in [Figure 7A–7C](#), the simulated case was, on average, 4.8°C warmer than the test box because the roof would produce, on average 8.7 W/m² less cooling during 24-h cycles. The absence of radiative cooling from the roof reduced the soffit's cooling effect on the interior air, with 11.5 W/m² less cooling at night, and 7.0 W/m² less cooling during the daytime. The interior air temperature nevertheless remained cooler than the reference case (with an insulated roof) because it benefited from conductive cooling from the nighttime ambient temperatures. We also carried out the same analysis but simulating 20 times more mass in the roof. In that case, the interior air would be on average 5.6°C cooler under a roof with radiative cooling than without (see [Figure 7D](#) and [7E](#)). The cooling loads from the soffit would decrease by 3.5, 3.5, and 3.4 W/m² during the night, daytime, and diurnal period, respectively, compared to an equivalent massive roof with a thermal emissivity of $\epsilon = 0.92$ (see [Figure 7F](#)). Without radiative cooling, the additional thermal mass in the roof would stabilize the interior temperature but raise it around the daily mean ambient temperature.

Latent heat phenomena

Forty-two 28-g silica gel desiccant bags were placed inside the convection guard (under the PE film and around the radiator) to eliminate condensation on the radiator. To verify that the desiccant bags worked, we calculated the dew-point temperature (T_{dp}) from the ambient humidity and air temperature measured during the experiment and identified periods when condensation could have occurred ($T_{dp} > T_R$). Ambient humidity was higher during the first 4 days of the experiment, and the radiator temperature (T_R) was cooler than T_{dp} for 647 min/day on average during that period. During the other 10 days, $T_{dp} > T_R$ occurred only for an average of 81 min/day. [Figure 8A](#) shows the variations of T_{dp} and T_R for two typical days with a high potential of condensation and two typical days when the potential of condensation was minimal.

We calculated the latent heat of condensation over those 4 days as $LE = h_v (e_{amb} - e_{rad})/\xi$ where $L = 2.26$ MJ/kg is the latent heat of water, E is the rate of condensation, h_v is the diffusion coefficient of water vapor in air, e_{amb} is the actual ambient water pressure, e_{rad} is the saturation vapor pressure at temperature T_R , and $\xi = 66$ Pa/K is the psychrometric constant.^{68,69} In [Figure 8B](#), we compare the latent heat of condensation with the heat flux measurement on the radiator. These calculations show that, despite LE being considerable when the potential of condensation was high (November 13–15), the pattern of heat exchange on the radiator is similar to the periods when LE was low or non-existent (November 23–25). If latent heat exchange did occur, it would have dominated the energy balance and changed the temperature evolution of the radiator and the interior during these time windows. Because there is no sign of this occurring, we conclude that the desiccant worked, preventing condensation and eliminating latent heat exchange effects on the radiator during the experiment. From the trends shown in [Figure 8A](#), we also predict that increasing the roof's thermal mass, as suggested above, would have

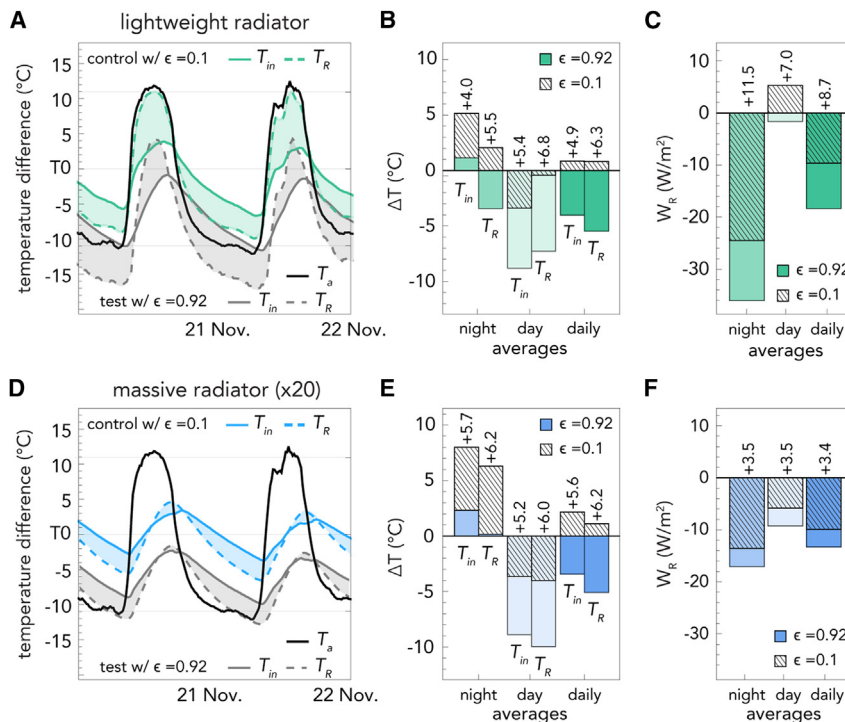


Figure 7. Isolating the effects of radiative cooling

(A) Typical variations of T_{in} , T_R , and T_a relative to the mean ambient temperature $T0 = (T_{a,max} - T_{a,min})/2$ for 2 days in November 2022 for a simulated control case where the uninsulated roof is the same as in the test box but with a thermal emissivity (ϵ) of 10%. The solid and dashed gray curves are the interior (T_{in}) and radiator temperature (T_R) measured in the test box. The black curve is the measured ambient temperature.

(B) Comparison of the nighttime, daytime, and daily average temperature differences with the ambient temperature between the test box with radiative cooling ($\epsilon = 0.92$) and the simulated control ($\epsilon = 0.1$).

(C) Comparison of the nighttime, daytime, and daily average heat flux on the soffit of the test box with and without radiative cooling.

(D) Typical variations of T_{in} , T_R , and T_a relative to the mean ambient temperature $T0$ for 2 days in November 2022 for simulated control cases where the uninsulated roof is 20 times thicker and has a thermal emissivity (ϵ) of 10%. The solid and dashed gray curves are the interior (T_{in}) and radiator temperature predictions for a massive roof with $\epsilon = 0.92$. The black curve is the measured ambient temperature.

(E) Comparison of the nighttime, daytime, and daily average temperature differences with the ambient temperature between a box with a massive roof and radiative cooling ($\epsilon = 0.92$) and a box with a massive roof but no radiative cooling ($\epsilon = 0.1$).

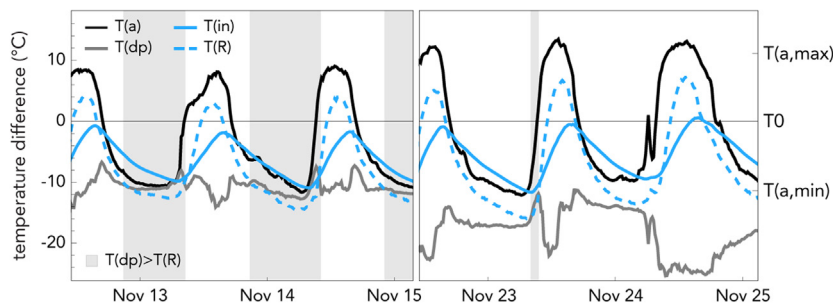
(F) Comparison of the nighttime, daytime, and daily average heat flux on the soffit of a massive roof with and without radiative cooling.

further reduced the likelihood of condensation because the more stable radiator temperature would have been less likely to drop below the dew-point temperature.

ACKNOWLEDGMENTS

We would like to thank John May and Zeina Koreitem for hosting the experiment, Michael Scarborough for help with on-site maintenance, and Victoria Desgagné for help with designing and assembling the test boxes. S.C. acknowledges support from the Canada Foundation for Innovation (2020 CFI Innovation Fund), McGill Sustainability Systems Initiative (MSSI), and the Natural Sciences and Engineering Research Council of Canada (NSERC Discovery Grant) under grant no. RGPIN-2022-04490. A.P.R. acknowledges support from the National Science Foundation

A



B

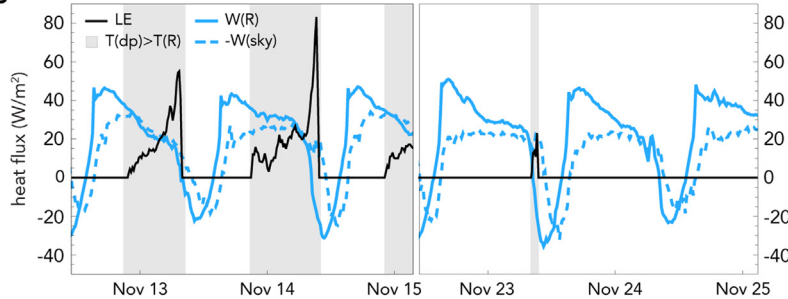


Figure 8. Verifying the negligible effects of condensation on the radiator

(A) Typical variations of T_{in} , T_R , and T_{dp} relative to the mean ambient temperature T_0 for 2 days when the potential of condensation is high (November 13–15) and 2 days when the potential of condensation is minimal (November 23–25). The black curve is the measured ambient temperature (T_a) and the gray areas indicate the period when the radiator temperature (T_R) is cooler than the dew-point temperature (T_{dp}).

(B) Comparison of the latent heat of condensation (LE) with the heat flux measurements on the sky-facing (W_{sky}), and soffit (W_R) side of the radiator. Since the patterns in the heat flux measurements are similar despite considerable differences in LE , we conclude that the experiment design was successful at eliminating the effect of latent heat phenomena on the radiator.

(NSF CAREER) under grant no. 2146577 and the Sloan Research Fellowship (Alfred P. Sloan Foundation).

AUTHOR CONTRIBUTIONS

Conceptualization, S.C.; methodology, R.F. and S.C.; formal analysis, R.F. and S.C.; investigation, R.F.; resources, J.M. and A.P.R.; data curation, R.F.; writing – original draft, R.F. and S.C.; writing – review & editing, S.C., J.M., and A.P.R.; visualization, R.F.; funding acquisition, S.C.; supervision, S.C.

DECLARATION OF INTERESTS

The authors declare no competing interests.

INCLUSION AND DIVERSITY

We support inclusive, diverse, and equitable conduct of research.

Received: April 19, 2023

Revised: July 20, 2023

Accepted: August 14, 2023

Published: September 5, 2023

REFERENCES

1. Davis, L.W., and Gertler, P.J. (2015). Contribution of air conditioning adoption to future energy use under global warming. *Proc. Natl. Acad. Sci. USA* 112, 5962–5967. <https://doi.org/10.1073/pnas.1423558112>.
2. IEA (2018). The Future of Cooling (IEA). License: CC BY 4.0. <https://www.iea.org/reports/the-future-of-cooling>.
3. Santamouris, M. (2016). Cooling the buildings – past, present and future. *Energy Build.* 128, 617–638. <https://doi.org/10.1016/j.enbuild.2016.07.034>.
4. McLinden, M.O., Seeton, C.J., and Pearson, A. (2020). New refrigerants and system configurations for vapor-compression refrigeration. *Science* 370, 791–796. <https://doi.org/10.1126/science.abe3692>.
5. Li, T., Zhai, Y., He, S., Gan, W., Wei, Z., Heidarinejad, M., Dalgo, D., Mi, R., Zhao, X., Song, J., et al. (2019). A radiative cooling structural material. *Science* 364, 760–763. <https://doi.org/10.1126/science.aau9101>.
6. Mandal, J., Yang, Y., Yu, N., and Raman, A.P. (2020). Paints as a Scalable and Effective Radiative Cooling Technology for Buildings. *Joule* 4, 1350–1356. <https://doi.org/10.1016/j.joule.2020.04.010>.
7. Han, D., Fei, J., Mandal, J., Liu, Z., Li, H., Raman, A.P., and Ng, B.F. (2022). Sub-ambient radiative cooling under tropical climate using highly reflective polymeric coating. *Sol. Energy Mater. Sol. Cell.* 240, 111723. <https://doi.org/10.1016/j.solmat.2022.111723>.
8. Mandal, J., Fu, Y., Overvig, A.C., Jia, M., Sun, K., Shi, N.N., Zhou, H., Xiao, X., Yu, N., and Yang, Y. (2018). Hierarchically porous polymer coatings for highly efficient passive daytime radiative cooling. *Science* 362, 315–319. <https://doi.org/10.1126/science.aat9513>.
9. Raman, A.P., Anoma, M.A., Zhu, L., Rephaeli, E., and Fan, S. (2014). Passive radiative cooling below ambient air temperature under direct sunlight. *Nature* 515, 540–544. <https://doi.org/10.1038/nature13883>.
10. Zhai, Y., Ma, Y., David, S.N., Zhao, D., Lou, R., Tan, G., Yang, R., and Yin, X. (2017). Scalable-manufactured randomized glass-polymer hybrid metamaterial for daytime radiative cooling. *Science* 355, 1062–1066. <https://doi.org/10.1126/science.aai7899>.
11. Huang, X., Mandal, J., and Raman, A.P. (2021). Do-it-yourself radiative cooler as a radiative cooling standard and cooling component for device design. *JPE* 12, 012112. <https://doi.org/10.1117/1.JPE.12.012112>.
12. Chen, Y., Mandal, J., Li, W., Smith-Washington, A., Tsai, C.-C., Huang, W., Shrestha, S., Yu, N., Han, R.P.S., Cao, A., and Yang, Y. (2020). Colored and paintable bilayer coatings with high solar-infrared reflectance for efficient cooling. *Sci. Adv.* 6, eaaz5413. [eaaz5413](https://doi.org/10.1126/sciadv.aaz5413). <https://doi.org/10.1126/sciadv.aaz5413>.
13. Zhao, D., Aili, A., Zhai, Y., Lu, J., Kidd, D., Tan, G., Yin, X., and Yang, R. (2019). Subambient Cooling of Water: Toward Real-World Applications of Daytime Radiative Cooling. *Joule* 3, 111–123. <https://doi.org/10.1016/j.joule.2018.10.006>.
14. Goldstein, E.A., Raman, A.P., and Fan, S. (2017). Sub-ambient non-evaporative fluid cooling with the sky. *Nat. Energy* 2, 17143–17147. <https://doi.org/10.1038/nenergy.2017.143>.
15. Wu, Y., Zhao, H., Sun, H., Duan, M., Lin, B., and Wu, S. (2022). A review of the application of radiative sky cooling in buildings: Challenges and optimization. *Energy Convers. Manag.* 265, 115768. <https://doi.org/10.1016/j.enconman.2022.115768>.
16. Fang, H., Zhao, D., Yuan, J., Aili, A., Yin, X., Yang, R., and Tan, G. (2019). Performance evaluation of a metamaterial-based new cool roof using improved Roof Thermal Transfer Value model. *Appl. Energy* 248, 589–599. <https://doi.org/10.1016/j.apenergy.2019.04.116>.
17. Gentle, A.R., and Smith, G.B. (2015). A Subambient Open Roof Surface under the Mid-Summer Sun. *Adv. Sci. 2*, 1500119. <https://doi.org/10.1002/advs.201500119>.
18. Santamouris, M. (2014). Cooling the cities – A review of reflective and green roof mitigation technologies to fight heat island and improve comfort in urban environments. *Sol. Energy* 103, 682–703. <https://doi.org/10.1016/j.solener.2012.07.003>.
19. Zhao, D., Aili, A., Zhai, Y., Xu, S., Tan, G., Yin, X., and Yang, R. (2019). Radiative sky cooling: Fundamental principles, materials, and applications. *Appl. Phys. Rev.* 6, 021306. <https://doi.org/10.1063/1.5087281>.
20. Erell, E. (2013). *Roof Cooling Techniques: A Design Handbook* (Routledge).
21. Synnefa, A., Santamouris, M., and Livada, I. (2006). A study of the thermal performance of reflective coatings for the urban environment. *Sol. Energy* 80, 968–981. <https://doi.org/10.1016/j.solener.2005.08.005>.
22. The Lancet COVID-19 Commission Task Force on Safe Work (2022). Safe School, and Safe Travel. Proposed Non-infectious Air Delivery Rates (NADR) for Reducing Exposure to Airborne Respiratory Infectious Diseases.
23. Bouet, P. (2021). A Silent Graph. Tracing the Algerian Past of French Solar Experiments. *abe*. <https://doi.org/10.4000/abe.8913>.
24. Trombe, F. (1967). Devices for Lowering the Temperature of a Body by Heat Radiation Therefrom.
25. Bouet, P. (2022). *Domestiquer l'énergie solaire* Architecture, décolonisation et écologisme dans la France d'après-guerre (Université Gustave Eiffel: Doctoral thesis), pp. 1945–1986.
26. Heo, S.-Y., Lee, G.J., Kim, D.H., Kim, Y.J., Ishii, S., Kim, M.S., Seok, T.J., Lee, B.J., Lee, H., and Song, Y.M. (2020). A Janus emitter for passive heat release from enclosures. *Sci. Adv.* 6, eabb1906. <https://doi.org/10.1126/sciadv.eabb1906>.
27. Givoni, B. (1994). *Passive Low Energy Cooling of Buildings* (John Wiley & Sons).
28. Hay, H.R., and Yellott, J.I. (1969). International aspects of air conditioning with movable insulation. *Sol. Energy* 12, 427–438. [https://doi.org/10.1016/0038-092X\(69\)90065-6](https://doi.org/10.1016/0038-092X(69)90065-6).
29. M. Santamouris, ed. (2007). *Advances in Passive Cooling* (Routledge). <https://doi.org/10.4324/9781849773966>.
30. Holford, J.M., and Woods, A.W. (2007). On the thermal buffering of naturally ventilated buildings through internal thermal mass. *J. Fluid Mech.* 580, 3–29. <https://doi.org/10.1017/S0022112007005320>.
31. Lishman, B., and Woods, A.W. (2009). The effect of gradual changes in wind speed or heat load on natural ventilation in a thermally massive building. *Build. Environ.* 44, 762–772. <https://doi.org/10.1016/j.buildenv.2008.06.026>.
32. Craig, S. (2019). The optimal tuning, within carbon limits, of thermal mass in naturally ventilated buildings. *Build. Environ.* 165, 106373. <https://doi.org/10.1016/j.buildenv.2019.106373>.
33. De Toldi, T., Craig, S., and Sushama, L. (2022). Internal thermal mass for passive cooling and ventilation: adaptive comfort limits, ideal quantities, embodied carbon. *Build. Cities* 3, 42–67. <https://doi.org/10.5334/bc.156>.
34. Cuce, P.M., and Riffat, S. (2016). A state of the art review of evaporative cooling systems for building applications. *Renew. Sustain. Energy Rev.* 54, 1240–1249. <https://doi.org/10.1016/j.rser.2015.10.066>.
35. Chenvidyakarn, T. (2013). *Buoyancy Effects on Natural Ventilation* (Cambridge University Press).
36. Linden, P.F., Lane-Serff, G.F., and Smeed, D.A. (1990). Emptying filling boxes: the fluid mechanics of natural ventilation. *J. Fluid Mech.* 212, 309–335. <https://doi.org/10.1017/S0022112090001987>.
37. Fitzgerald, S.D., and Woods, A.W. (2008). The influence of stacks on flow patterns and stratification associated with natural ventilation. *Build. Environ.* 43, 1719–1733. <https://doi.org/10.1016/j.buildenv.2007.10.021>.
38. Gladstone, C., and Woods, A.W. (2001). On buoyancy-driven natural ventilation of a room with a heated floor. *J. Fluid Mech.* 441, 293–314. <https://doi.org/10.1017/S0022112001004876>.
39. Evangelisti, L., Guattari, C., and Asdrubali, F. (2019). On the sky temperature models and their influence on buildings energy performance: A critical review. *Energy Build.* 183, 607–625. <https://doi.org/10.1016/j.enbuild.2018.11.037>.
40. ASHRAE (2017). *ANSI/ASHRAE Standard 55-2017: Thermal Environmental Conditions for Human Occupancy (ASHRAE)*.
41. Parkinson, T., de Dear, R., and Brager, G. (2020). Nudging the adaptive thermal comfort model. *Energy Build.* 206, 109559. <https://doi.org/10.1016/j.enbuild.2019.109559>.

42. Vellei, M., de Dear, R., Inard, C., and Jay, O. (2021). Dynamic thermal perception: A review and agenda for future experimental research. *Build. Environ.* 205, 108269. <https://doi.org/10.1016/j.buildenv.2021.108269>.
43. Ashby, M.F. (2013). *Materials and the Environment: Eco-Informed Material Choice*, 2nd ed. (Elsevier/Butterworth-Heinemann).
44. Chenvidyakarn, T., and Woods, A. (2005). Top-down precooled natural ventilation. *Build. Serv. Eng. Res. Technol.* 26, 181–193. <https://doi.org/10.1191/0143624405bt129oa>.
45. Livermore, S.R., and Woods, A.W. (2008). On the effect of distributed cooling in natural ventilation. *J. Fluid Mech.* 600, 1–17. <https://doi.org/10.1017/S0022112007009809>.
46. Bejan, A. (2013). *Convection Heat Transfer*, Fourth edition (Wiley).
47. Nellis, G., and Klein, S.A. (2009). *Heat Transfer* (Cambridge University Press).
48. Parker, D.A., Burridge, H.C., Partridge, J.L., Hacker, J.N., and Linden, P.F. (2021). Vertically distributed wall sources of buoyancy. Part 2. Unventilated and ventilated confined spaces. *J. Fluid Mech.* 907, A16. <https://doi.org/10.1017/jfm.2020.809>.
49. Peeters, L., Beausoleil-Morrison, I., and Novoselac, A. (2011). Internal convective heat transfer modeling: Critical review and discussion of experimentally derived correlations. *Energy Build.* 43, 2227–2239. <https://doi.org/10.1016/j.enbuild.2011.05.002>.
50. Dascalaki, E., Santamouris, M., Balaras, C.A., and Asimakopoulos, D.N. (1994). Natural convection heat transfer coefficients from vertical and horizontal surfaces for building applications. *Energy Build.* 20, 243–249. [https://doi.org/10.1016/0378-7788\(94\)90027-2](https://doi.org/10.1016/0378-7788(94)90027-2).
51. Fohanno, S., and Polidori, G. (2006). Modelling of natural convective heat transfer at an internal surface. *Energy Build.* 38, 548–553. <https://doi.org/10.1016/j.enbuild.2005.09.003>.
52. Khalifa, A.-J.N. (2001). Natural convective heat transfer coefficient – a review: II. Surfaces in two- and three-dimensional enclosures. *Energy Convers. Manag.* 42, 505–517. [https://doi.org/10.1016/S0196-8904\(00\)00043-1](https://doi.org/10.1016/S0196-8904(00)00043-1).
53. Zhang, J., Yuan, J., Liu, J., Zhou, Z., Sui, J., Xing, J., and Zuo, J. (2021). Cover shields for sub-ambient radiative cooling: A literature review. *Renew. Sustain. Energy Rev.* 143, 110959. <https://doi.org/10.1016/j.rser.2021.110959>.
54. Zhou, M., Song, H., Xu, X., Shahsafi, A., Qu, Y., Xia, Z., Ma, Z., Kats, M.A., Zhu, J., Ooi, B.S., et al. (2021). Vapor condensation with daytime radiative cooling. *Proc. Natl. Acad. Sci. USA* 118, e2019292118. <https://doi.org/10.1073/pnas.2019292118>.
55. Li, J., Wang, X., Liang, D., Xu, N., Zhu, B., Li, W., Yao, P., Jiang, Y., Min, X., Huang, Z., et al. (2022). A tandem radiative/evaporative cooler for weather-insensitive and high-performance daytime passive cooling. *Sci. Adv.* 8, eabq0411. <https://doi.org/10.1126/sciadv.abq0411>.
56. Geyer, F., D'Acunzi, M., Sharifi-Aghili, A., Saal, A., Gao, N., Kaltbeitzel, A., Sloot, T.-F., Berger, R., Butt, H.-J., and Vollmer, D. (2020). When and how self-cleaning of superhydrophobic surfaces works. *Sci. Adv.* 6, eaaw9727. <https://doi.org/10.1126/sciadv.aaw9727>.
57. Song, J., Zhang, W., Sun, Z., Pan, M., Tian, F., Li, X., Ye, M., and Deng, X. (2022). Durable radiative cooling against environmental aging. *Nat. Commun.* 13, 4805. <https://doi.org/10.1038/s41467-022-32409-7>.
58. Im, E.-S., Pal, J.S., and Eltahir, E.A.B. (2017). Deadly heat waves projected in the densely populated agricultural regions of South Asia. *Sci. Adv.* 3, e1603322. <https://doi.org/10.1126/sciadv.1603322>.
59. Mora, C., Dousset, B., Caldwell, I.R., Powell, F.E., Geronimo, R.C., Bielecki, C., Counsell, C.W.W., Dietrich, B.S., Johnston, E.T., Louis, L.V., et al. (2017). Global risk of deadly heat. *Nat. Clim. Change* 7, 501–506. <https://doi.org/10.1038/nclimate3322>.
60. Sadeghi, M., de Dear, R., Morgan, G., Santamouris, M., and Jalaludin, B. (2021). Development of a heat stress exposure metric – Impact of intensity and duration of exposure to heat on physiological thermal regulation. *Build. Environ.* 200, 107947. <https://doi.org/10.1016/j.buildenv.2021.107947>.
61. Morawska, L., Allen, J., Bahnfleth, W., Bluyssen, P.M., Boerstra, A., Buonanno, G., Cao, J., Dancer, S.J., Floto, A., Franchimon, F., et al. (2021). A paradigm shift to combat indoor respiratory infection. *Science* 372, 689–691. <https://doi.org/10.1126/science.abg2025>.
62. Khosla, R., Miranda, N.D., Trotter, P.A., Mazzone, A., Renaldi, R., McElroy, C., Cohen, F., Jani, A., Perera-Salazar, R., and McCulloch, M. (2020). Cooling for sustainable development. *Nat. Sustain.* 4, 201–208. <https://doi.org/10.1038/s41893-020-00627-w>.
63. Teitelbaum, E., Chen, K.W., Aviv, D., Bradford, K., Ruefenacht, L., Sheppard, D., Teitelbaum, M., Meggers, F., Pantelic, J., and Rysanek, A. (2020). Membrane-assisted radiant cooling for expanding thermal comfort zones globally without air conditioning. *Proc. Natl. Acad. Sci. USA* 117, 21162–21169. <https://doi.org/10.1073/pnas.2001678117>.
64. Suerich-Gulick, F., Halepaska, A., and Craig, S. (2021). Cascading Temperature Demand: The Limits of Thermal Nesting in Naturally Ventilated Buildings (Building and Environment), 108607. <https://doi.org/10.1016/j.buildenv.2021.108607>.
65. Teitelbaum, E., Jayathissa, P., Miller, C., and Meggers, F. (2020). Design with Comfort: Expanding the psychrometric chart with radiation and convection dimensions. *Energy Build.* 209, 109591. <https://doi.org/10.1016/j.enbuild.2019.109591>.
66. Teitelbaum, E., Alsaad, H., Aviv, D., Kim, A., Voelker, C., Meggers, F., and Pantelic, J. (2022). Addressing a systematic error correcting for free and mixed convection when measuring mean radiant temperature with globe thermometers. *Sci. Rep.* 12, 6473. <https://doi.org/10.1038/s41598-022-10172-5>.
67. Idel'chik, I.E., and Ginevskii, A.S. (2007). *Handbook of Hydraulic Resistance* (Begell House), 4th ed. rev. and augmented.
68. Nilsson, T.M.J., Vargas, W.E., Niklasson, G.A., and Granqvist, C.G. (1994). Condensation of water by radiative cooling. *Renew. Energy* 5, 310–317. [https://doi.org/10.1016/0960-1481\(94\)90388-3](https://doi.org/10.1016/0960-1481(94)90388-3).
69. Monteith, J.L. (2013). *Principles of Environmental Physics*, 4th ed. (Academic Press).